Tuning the Site-to-Site Interaction in Ru–M (M = Co, Fe, Ni) Di-atomic Electrocatalysts to Climb up the Volcano Plot of Oxygen Electroreduction

Mengjie Liu,[1] Hoje Chun,[2] Tsung-Cheng Yang,[3] Sung Jun Hong,[2] Chia-Min Yang,[3,4,]* Byungchan Han,[2,]* and Lawrence Yoon Suk Lee[1,5,]*

[1] Department of Applied Biology and Chemical Technology and the State Key Laboratory of Chemical Biology and Drug Discovery, The Hong Kong Polytechnic University, Hung Hom, Kowloon, Hong Kong SAR, China

[2] Department of Chemical and Biomolecular Engineering, Yonsei University, Seoul 03722, Republic of Korea

[3] Department of Chemistry, National Tsing Hua University, Hsinchu 300034, Taiwan

[4] Frontier Research Center on Fundamental and Applied Sciences of Matters, National Tsing Hua University, Hsinchu 300034, Taiwan

[5] Research Institute for Smart Energy, The Hong Kong Polytechnic University, Hung Hom, Kowloon, Hong Kong SAR, China

ABSTRACT:

The modulating of the geometric and electronic structures of metal–N–C atomic catalysts for improving their performance in catalyzing oxygen reduction reaction (ORR) is highly desirable yet challenging. We herein report a delicate "encapsulation–substitution" strategy for the synthesis of paired metal sites in N-doped carbon. With the regulation of d-orbital energy level, a significant increment in oxygen electroreduction activity was demonstrated in Ru–Co di-atomic catalyst (DAC) compared with other di-atomic (Ru–Fe and Ru–Ni) and single-atomic counterparts. The Ru–Co DAC efficiently reduces oxygen with a halfwave potential of 0.895 V $vs.$ RHE and a turnover frequency of 2.424 s^{-1} at 0.7 V, establishing optimal thermodynamic and kinetic behaviors in the triple-phase reaction under practical conditions. Moreover, the Ru–Co DAC electrode displays bifunctional activity in gas diffusion Zn–air battery with a small voltage gap of 0.603 V, outperforming the commercial Pt/C|RuO$_2$ catalyst. Our findings provide a clear understanding of site-to-site interaction on ORR and a benchmark evaluation of atomic catalysts with correlations of di-atomic structure, energy level, and overall catalytic performance at the sub-nanometer level.

KEYWORDS: di-atomic catalyst; electrocatalysis; oxygen reduction reaction; d-band center; zinc–air battery

1. Introduction

Single atomic catalysts (SACs) have emerged as potential alternatives to precious-metal-based catalysts in various heterogeneous catalytic reactions.[1-4] In particular, the metal–X–C (X = N, P, and S) moieties immobilized on a carbon substrate represent a typical atom-economic catalyst that delivers ultrahigh site utilization, remarkable activity, selectivity, and durability, thereby qualifying them as the new breed of cutting-edge systems in electrocatalytic oxygen reduction reaction (ORR).[5, 6] SACs have received widespread attention and shown great performances in metal–air batteries and proton-conducting membrane fuel cells, which are distinct from their bulk or nanosized counterparts, but challenges still remain.[7, 8] Recent research activities on SACs have mainly focused on solving practical problems of single atoms; either enhancing the activity by regulating the electronic structure and local coordination environments[9-12] or achieving the production of high single-atom concentration.[13, 14] More recently, the rational manipulation of binuclear metallic sites has surged as a new effective way of designing synergistic effect that can boost the reaction activity and selectivity of isolated atomic sites, and it has even reshaped the understanding of reaction mechanism.[15-19] However, such an exploration heavily relies on the ideal atomic structure and therefore requires an accurate synthetic strategy to ensure precise site distribution.

Zeolitic imidazolate frameworks-8 (ZIF-8), a subclass of metal–organic frameworks, owns atomic-scale metal nodes and built-in molecular-scale cavities at the same time.[18, 20] Such unique structural features of ZIF-8 allow the possibility of uniformly creating neighboring metal dimer by: 1) *in situ* encapsulation of cage-separated metal precursor and the appropriate substitution of a coordinated metal node can provide the source of the adjacent binuclear site; 2) the chelating effect of nitrogen species, which may be converted from the organic templates, can produce metal–

N coordination in the carbon skeleton; and 3) the low boiling-point zinc nodes evaporate during calcination, which guarantees the isolated distribution of dimeric metal sites. Such merits of ZIF-8 make it an appropriate platform for the precise construction of binuclear sites and thereby enable the exploration of atomic activity.

Among the platinum-group metals that exhibit outstanding performances in oxygen-involved catalysis (ORR and oxygen evolution reaction: OER),[21, 22] ruthenium (Ru) enjoys a relatively advantageous position in terms of price ($379 per oz) over the others, such as Pt ($1,010 per oz), Ir ($3,032 per oz), and Pd ($2,294 per oz).[23] However, according to some previous theoretical and experimental results, the strong binding of reactants onto Ru during oxygen-involved catalysis causes an energetically unfavorable step.[24, 25] The regulation of intrinsic spin state and d-orbital can effectively tune the adsorption/desorption behavior of key intermediates on the surface of Ru, shifting the position of Ru to the top of the Volcano plot. One feasible approach is to couple the Ru with another $3d$ transition metal possessing the electron-donating nature, which is located on the weak bonding leg of the Volcano plot, such as Co, Fe, and Ni. With the precise site control of two metal atoms, such modulation by $3d$ metal can also offer atomic economy by reducing the loading of Ru atoms.

With these considerations, we prepared a series of heteronuclear Ru–M pairs supported on N-doped ordered macroporous carbon (RuMN$_x$/C, M = Co, Fe, and Ni) using a ZIF-8 template in the "precursor encapsulation–node substitution" strategy. The role of well-defined metal dimers on the oxygen reduction activity is systematically interpreted by X-ray absorption spectroscopy and the analysis of kinetic and thermodynamic behaviors during the electrochemical process. Theoretical simulations provide the atomic understanding of catalytic performance enhancement, which verifies the effectiveness of modulating the electronic structure and energy levels by the $3d$

metal atoms. In particular, RuCoN$_x$/C exhibits distinguished ORR/OER activities with a low voltage gap of 0.603 V when assembled as a zinc–air battery, which demonstrates the potential of M–N–C catalysts in practical energy conversion applications. The delicate design, structural identification, and catalytic behavior of RuMN$_x$/C catalysts are discussed to provide fundamental insights into the correlation between the atomic-scale structure and the catalytic process.

Results and Discussion
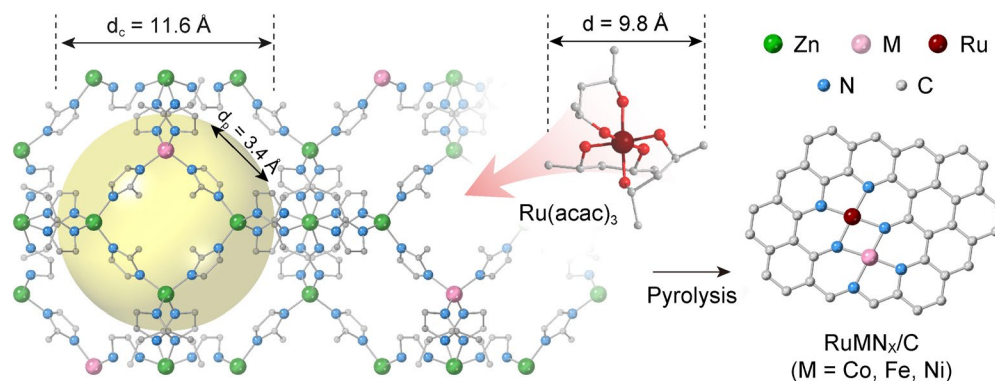
Figure 1. A schematic diagram illustrating the synthetic strategy of RuMN$_x$/C. d$_c$, d$_p$, and d indicate the diameter of cavity (ZIF-8), aperture (ZIF-8), and Ru(acac)$_3$ molecule, respectively.

Figure 1 illustrates the design strategies of "trace metal substitution" and "cavity-separated precursor encapsulation" for the preparation of RuMN$_x$/C. During the solvothermal synthesis of ZIF-8 using close-packed polystyrene (PS) monoliths (average d = 176 nm, **Figure S1**) as the hard template,[9] selected metal ions (M^{n+} = Co^{2+}, Fe^{3+}, and Ni^{2+}) were introduced to substitute Zn and form M-doped-ZIFs.[26, 27] At the same time, Ru(acac)$_3$, which is selected as the Ru precursor because of its size (9.8 Å) smaller than the central cavities (d = 11.6 Å) but larger than the apertures (d = 3.4 Å) of ZIF-8, is accommodated in the cavities of *in situ* formed ZIFs.[2, 18] The removal of PS template by rinsing with DMF affords M-doped-ZIFs encasing the Ru(acac)$_3$ (Ru@ZnM-ZIFs, **Figure S2**), and the subsequent pyrolysis at 950 °C in H$_2$/Ar atmosphere selectively evaporates Zn

atoms, leaving the Ru and M sites embedded in the N-doped carbon matrix that is derived from the organic linkers and ligands of Ru@ZnM-ZIFs. By adjusting the concentrations of M and Ru(acac)$_3$, Ru–M binuclear sites are constructed from the isolated pairs of Ru(acac)$_3$ and M node without forming aggregated metallic particles.

The powder X-ray diffraction (PXRD) patterns (**Figure S3**) of the as-prepared RuMN$_x$/C samples show two broad peaks at around 25 and 43°, which correspond to the (002) and (100) planes of graphite, respectively. No signals of clusters or nanoparticles are observed from any samples. Electron microscopic techniques were utilized to probe the morphology and atomic structure of RuMN$_x$/C samples. The representative transmission electron microscopic (TEM) image (**Figure 2a**) and the high-angle annular dark-field scanning TEM (HAADF-STEM) image (**Figure 2b**) reveal the truncated rhombic dodecahedral carbon skeleton of RuCoN$_x$/C, the morphology of which is inherited from the ZIF-8. The periodic macropores (average $d = 176$ nm), which are the negative replicates of PS monoliths and can offer the diffusion/transport channels for reactants and products for catalysis, are evident in the polyhedron. The HAADF-STEM images of other RuMN$_x$/C samples exhibit similar macroporous structural features (**Figures S4** and **S5**), which validates the universality of the PS-assisted synthetic strategy. The elemental mapping images in **Figure 2c** indicate the uniform dispersion of Ru, Co, and N over the entire carbon skeleton of RuCoN$_x$/C. Aberration-corrected HAADF-STEM was used to precisely identify the existence of dimeric metal sites in the RuCoN$_x$/C. **Figures 2d** and **S6** display numerous bright dots on the carbon matrix, which correspond to Ru and Co atoms. A higher-magnification TEM image (**Figure 2e**) reveals that most metal atoms are paired as dimers with an average interatomic distance of 2.09 ± 0.25 Å, as determined by the statistical analysis of interactive 3D surface plots (**Figure 2f**) of 70 atomic pairs (**Figure 2g**).
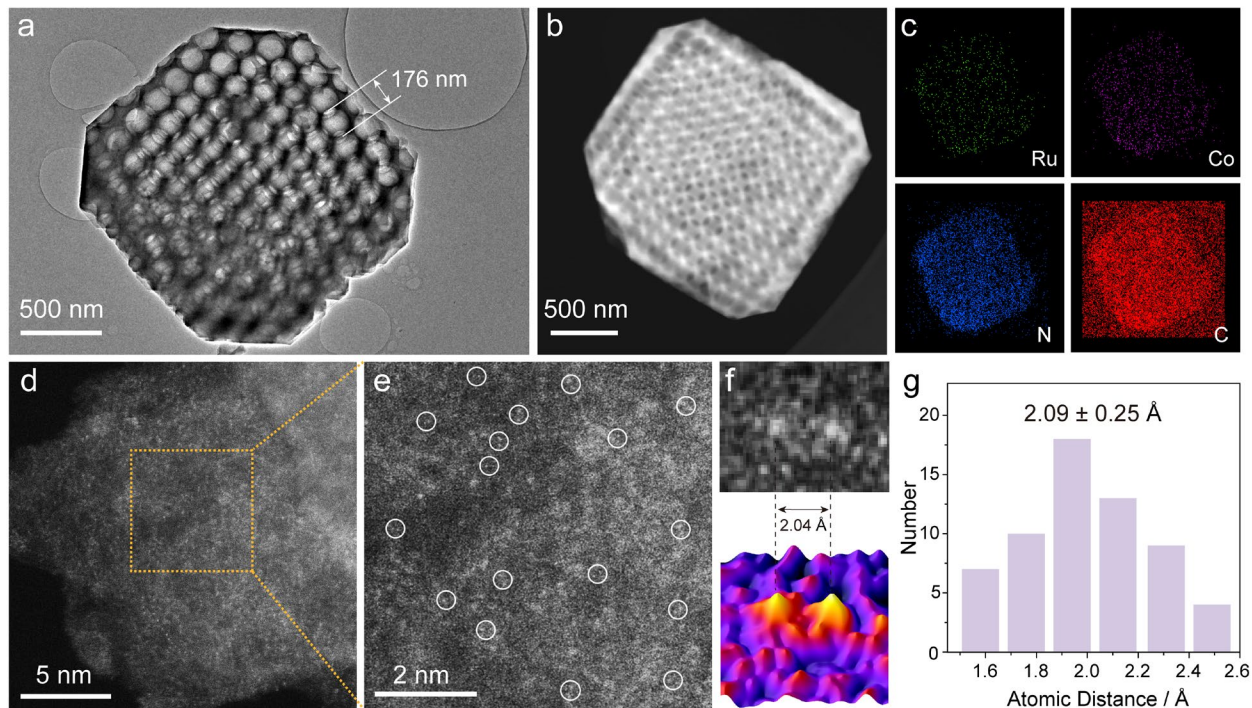
Figure 2. Structural characterizations of RuCoN$_x$/C. (a) Low-resolution TEM image; (b) HAADF-TEM image; (c) elemental mapping images; (d, e) aberration-corrected HAADF-STEM images; and (f) magnified image of an individual diatom in (e) and the corresponding 3D surface plot. White circles in (e) indicate di-atomic sites. (g) Interatomic distance distribution of 70 di-atomic sites.

The precise control of the amount of Ru and Co precursors is the key factor to ensure the homogenous dispersion of the di-atomic pairs. As the loading density of Ru/Co gradually increases in the Ru@ZnCo-ZIFs, the thermal migration and nucleation of metal atoms during pyrolysis can cause the aggregation of the metal nanoclusters or even larger particles. As shown in **Figures S7** and **S8**, when the ratio of Ru/Co precursors to Zn is increased from 1:100 to 2:100 or 3:100, a tiny metallic cluster (average d = 3 nm) or a large nanoparticle (d > 10 nm) embedded in N-doped carbon is formed, which are denoted as RuCo cluster and RuCo particle, respectively.
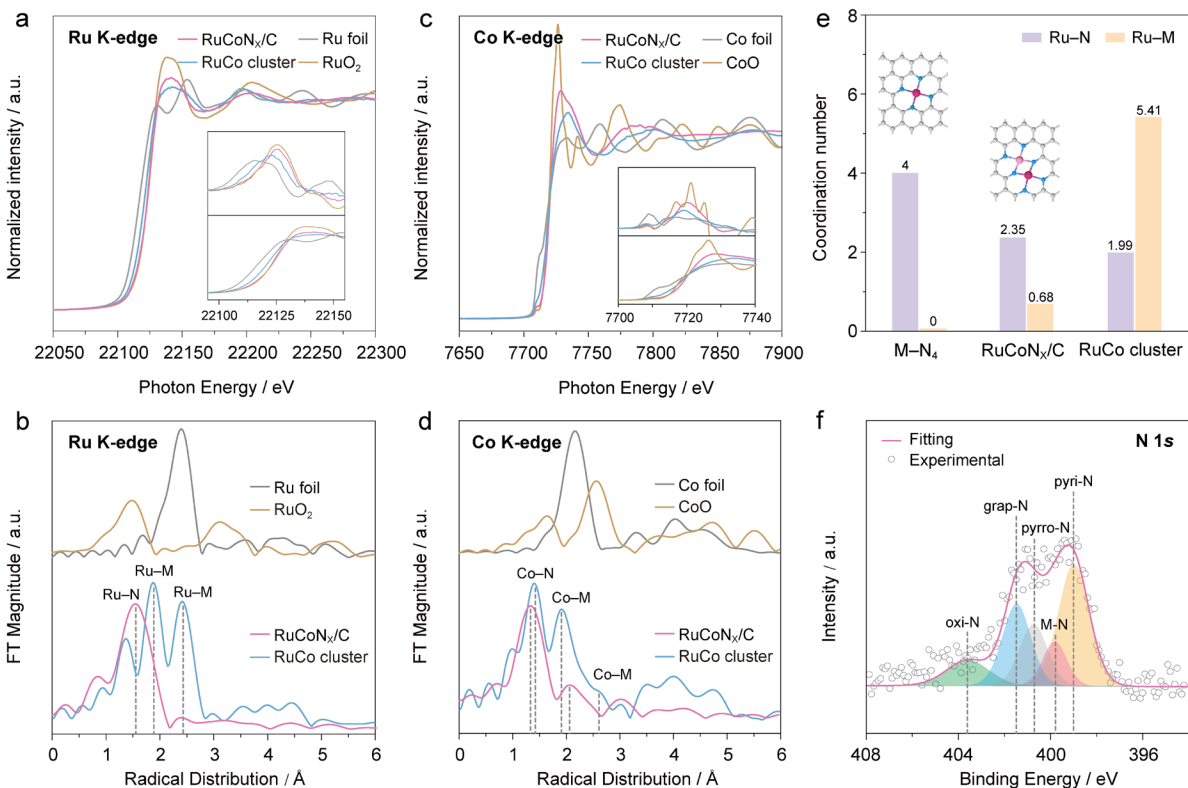
Figure 3. (a) Normalized Ru K-edge XANES spectra and (b) FT profiles of Ru K-edge k^2-weighted EXAFS data of RuCoN$_x$/C, RuCo cluster, RuO$_2$, and Ru foil without phase correction. (c) Normalized Co K-edge XANES spectra and (d) FT profiles of Co K-edge k^2-weighted EXAFS data of RuCoN$_x$/C, RuCo cluster, CoO, and Co foil without phase correction. Insets in (a) and (c) are the first derivative of XANES spectra (up) and the magnified absorption edge (down). (e) Fitted coordination numbers of Ru in ideal single atomic Ru–N$_4$, RuCoN$_x$/C, and RuCo cluster. (f) High-resolution N 1s XPS spectrum of RuCoN$_x$/C.

X-ray absorption spectroscopy (XAS) was engaged to investigate the coordination environment and chemical state of metal species in RuCoN$_x$/C. **Figure 3a** shows the Ru K-edge X-ray absorption near-edge structure (XANES) of RuCoN$_x$/C and three reference samples of RuCo clusters, RuO$_2$, and Ru foil. The absorption edge and white line of RuCoN$_x$/C are almost overlapping with those of RuO$_2$, indicating that the Ru sites in the RuCoN$_x$/C are mainly in +4 oxidation state. The RuCo cluster exhibits a negatively shifted absorption edge and white line located between those of RuO$_2$ and Ru foil, which suggests that the Ru sites in the cluster, on

average, also carry a positive but reduced charge. By linear fitting the Ru edge energies (**Figure S9a**), the average Ru oxidation states for RuCoN$_x$/C and RuCo cluster are calculated as 3.361 and 2.226, respectively. The k^2-weighted extended X-ray absorption fine structures (EXAFS) were Fourier transformed (FT), and the resulting profiles (**Figure 3b**, without phase correction) were further fitted to gain insights into the atomic configuration of dual atomic samples (**Figures S10** and **S11**). The profile of RuCoN$_x$/C (**Figure 3b**) displays the main peak at around 2.04 Å after phase correction (**Table S1**), which is assigned to the first shell of Ru–N coordination. The Ru–N signal is weaker in RuCo cluster, and two peaks at 2.28 Å and 2.78 Å, which are associated with the Ru–M scatterings in the different shells, are predominant.[28, 29] RuCoN$_x$/C displays the Ru–Co scattering at 2.20 Å, which is consistent with the previous microscopic results of a metallic dimer (**Figure 2g**).

Similar phenomena are observed in Co K-edge XANES and EXAFS profiles (**Figures 3c** and **3d**). The fitting of adsorption edge energies indicates that the average oxidation states for the Co sites in RuCoN$_x$/C and RuCo cluster are 1.824 and 1.626, respectively (**Figure S9b**). The Co K-edge EXAFS spectrum of RuCoN$_x$/C shows a major Co–N peak at 1.87 Å and an additional Co–M peak at 2.23 Å after phase correction (**Figure S11a** and **Table S2**), which is very close to the value of Ru–Co distance observed by HAADF-STEM (*cf*. **Figure 3f**) and that derived from Ru K-edge EXAFS data (2.20 Å, **Table S1**). In comparison, the RuCo cluster exhibits the more intense signals from the nearest (*ca*. 2.23 Å) and long-range (3~5 Å) Co–M paths. The XAS results obtained from RuFeN$_x$/C and RuNiN$_x$/C indicate the formation of Ru–M di-atomic structures, while RuN$_x$/C shows only single atomic features (**Figures S10** and **S11**).

The coordination environments of the two metals in RuCoN$_x$/C and RuCo cluster are further compared. The fitted Ru–M and Co–M coordination numbers (CNs) in RuCoN$_x$/C are 0.68 and

1.40, respectively, which are higher than that of the ideal isolated M–N$_4$ (0) but lower than those of the RuCo cluster (5.41 and 2.18). However, the CN values of M–N exhibit an opposite trend (**Figure 3e** and **Figure S12**). Especially, the CNs for the first shell of Ru–N and Co–N are 2.35 and 2.63 for RuCoN$_x$/C, which suggests that most metal atoms are coordinated in Ru–N$_3$ and Co–N$_3$ environment in a RuCoN$_6$ structure.

X-ray photoelectron spectroscopy (XPS) was employed to investigate the chemical state of surface species (**Figure S13**). All RuMN$_x$/C samples display similar N and C species (**Figures S14** and **S15**), mainly due to the same synthetic procedure. Typically, the high-resolution N 1s spectrum of RuCoN$_x$/C (**Figure 3f**) can be deconvoluted into four peaks that are ascribed to pyridinic N (399.0 eV), metal–N (399.8 eV), pyrrolic N (400.7 eV), and graphitic N (401.5 eV). Due to the presence of the O-containing precursor, Ru(acac)$_3$, a small peak of oxidized N species is also observed at 403.6 eV. The N species can anchor the metal atoms and also provide an active site for the subsequent catalytic reaction. The 3d spectra of metal species display no obvious signal except for the cluster sample, mainly due to their low content on the surface (**Figure S16**). The exact loading masses of Ru and Co in RuCoN$_x$/C are determined as 0.27 and 0.24 wt.%, respectively, by inductively coupled plasma optical emission spectrometry (ICP-OES, **Table S3**). Other samples contain similar amounts of active metal sites, which endows us with the possibility for precise estimation of catalytic performance.
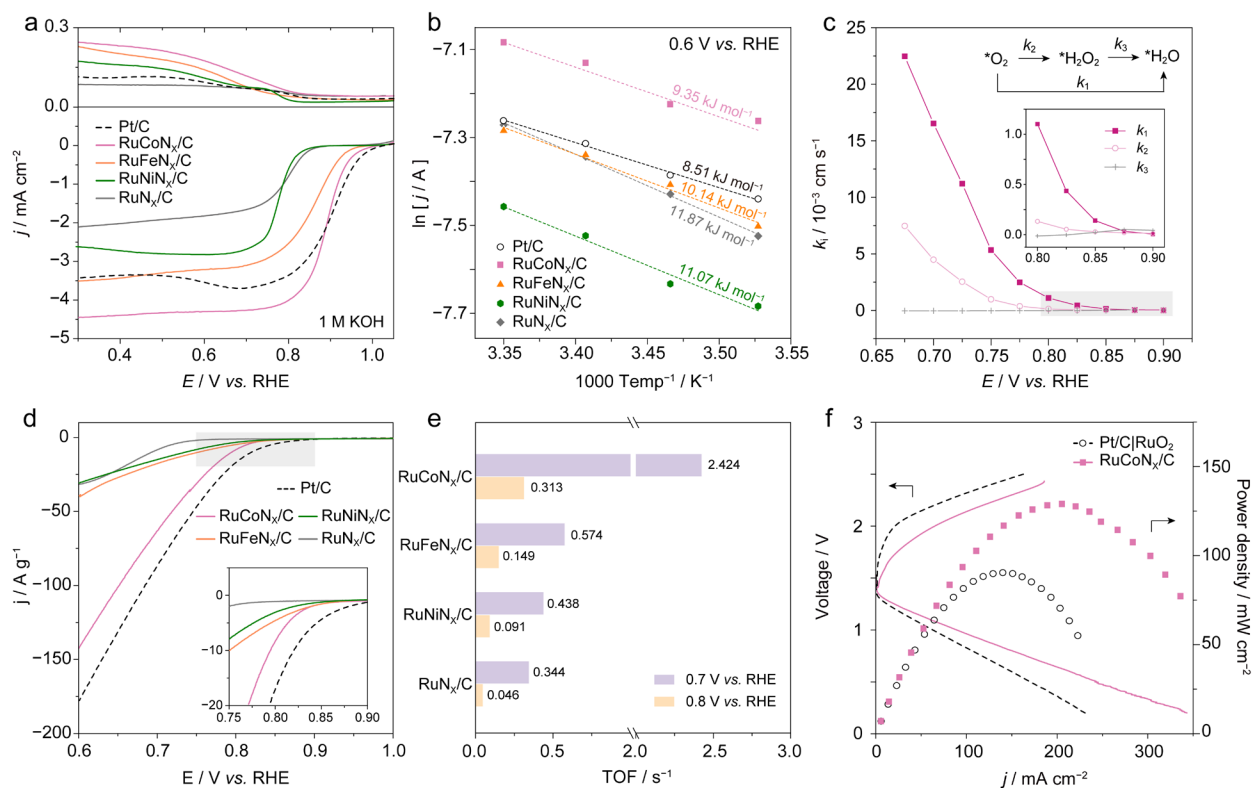
Figure 4. (a) RRDE voltammograms (upper: ring current; lower: disk current, without iR correction) and (b) Arrhenius plots of $RuMN_x/C$ and Pt/C. RRDE voltammetry was conducted at 1,600 rpm in O_2-saturated 1 M KOH, and the currents in (b) were collected at 0.6 V vs. RHE. (c) ORR rate constants (k_1, k_2, and k_3) of $RuCoN_x/C$ as a function of bias potential. Inset is the Damjanovic model. (d) Polarization curves measured in a gas diffusion flow cell and (e) normalized TOF values (at 0.8 and 0.7 V) of $RuMN_x/C$ and Pt/C. (f) Charge and discharge polarization curves of rechargeable Zn–air batteries constructed with $RuCoN_x/C$ and $Pt/C|RuO_2$ and the corresponding power density plots.

Electrocatalytic oxygen reduction performances of di-atomic structures were evaluated to demonstrate the effect of neighboring 3d metal atoms on the electronic configuration of Ru site. The onset potentials (E_{onset}) and half-wave potentials ($E_{1/2}$) of $RuMN_x/C$ were compared by linear sweep voltammetry (LSV, **Figures S17** and **S18**). $RuCoN_x/C$ affords E_{onset} and $E_{1/2}$ of 0.970 and 0.895 V vs. reversible hydrogen electrode (RHE), respectively, which are very close to those of Pt/C (0.975 and 0.895 V). $RuCoN_x/C$ also delivers a high diffusion-limited current density (j_L) of ca. 5.0 mA cm^{-2}, which is superior to Pt/C (ca. 4.2 mA cm^{-2}). Such performance of $RuCoN_x/C$

surpasses other analogues (RuFeN$_x$/C and RuNiN$_x$/C, **Figure S17**) as well as single atomic counterparts (RuN$_x$/C and CoN$_x$/C, **Figure S18**), following an activity trend of RuCoN$_x$/C > RuFeN$_x$/C ≈ CoN$_x$/C > RuNiN$_x$/C > RuN$_x$/C. All the dual atomic catalysts deliver enhanced ORR performances over the isolated Ru single atom, which highlights the key role of the secondary 3d metal in boosting the catalytic activity of Ru. **Figure 4a** compares the dual-electrode polarization curves of dual and single atomic catalysts, which were collected on a rotating ring disk electrode (RRDE) at 1,600 rpm in 1 M KOH saturated with O$_2$. The selectivity of catalysts can be accurately evaluated by calculating the electron transfer numbers (n) and peroxide yields (% HO$_2^-$) using RRDE polarization curves (**Note S1** and **Figure S20**). In a potential range between 0.3 and 0.8 V, all catalysts exhibit similar peroxide yields (10~25 %) and electron transfer numbers (3.5~3.8), which is an indication of the dominant 4e$^-$ reaction pathway and the suppressed side reaction.

The activation energies (E_a) of the RuMN$_x$/C catalysts toward ORR were evaluated at kinetic–diffusion mixed controlled region (0.6 V $vs.$ RHE)[12, 30] by Arrhenius Equation at temperatures ranging from 283.5 to 298.5 K (**Note S2** and **Figure S21**). **Figure 4b** compares the slopes of Arrhenius plots for RuMN$_x$/C catalysts with that of Pt/C, which represent E_a of 8.51, 9.35, 10.14, 11.07, and 11.87 kJ mol^{-1} for Pt/C, RuCoN$_x$/C, RuFeN$_x$/C, RuNiN$_x$/C, and RuN$_x$/C, respectively. The E_a values follow the activity trends determined by voltammetry, indicating that RuCoN$_x$/C possesses a similar energy barrier and intrinsic activity toward ORR as Pt/C.

The kinetic reaction order of RuMN$_x$/C catalysts was investigated by the Kouteck–Levich plots obtained using the LSV curves at various rotating speeds ranging from 625 to 2,025 rpm (**Note S3** and **Figure S22**). The first-order ORR reaction kinetics are suggested for all the RuMN$_x$/C catalysts by the linear relationship between the reciprocal of kinetic current density and the reciprocal square root of rotating speed. From the LSV curves, Tafel slopes are calculated as 89.2,

109.0, 118.6, and 116.4 mV dec^{-1} for RuCoN$_x$/C, RuFeN$_x$/C, RuNiN$_x$/C, and RuN$_x$/C, respectively, indicating the rapid kinetics of RuCoN$_x$/C during the reduction process is comparable to that of Pt/C (86.3 mV dec^{-1}, **Figure S17c**). By engaging RRDE voltammetry and the ideal Damjanovic model, the kinetics of each reaction pathway was further analyzed for RuCoN$_x$/C (**Note S4**, **Figure S23**, and **Table S4**).[31, 32] Three kinetic rate constants for ORR, k_1 for four-electron reduction from oxygen to water, k_2 for two-electron reduction from oxygen to peroxide, and k_3 for two-electron reduction from peroxide to water, are plotted against the bias potential in **Figure 4c**. Unlike the other two constants, k_1 displays a prevailing potential-dependent property in the initial charge transfer-dominated region (0.90~0.80 V) and the subsequent mass transfer-dominated region (0.80~0.65 V). k_2 shows slight increments until the bias gets much negative (< 0.75 V), while k_3 shows no changes in the entire potential window. These results well demonstrate the accelerated four-electron process and thereby suppressed peroxide reduction at RuCoN$_x$/C.

Figure S24 compares the Nyquist and Bode plots of RuMN$_x$/C and Pt/C catalysts obtained by electrochemical impedance spectroscopy (EIS) at 0.7 V (mass transfer-controlled region). In the high-frequency region of the Nyquist plot, all catalysts display similar semicircles of *ca*. 10 Ω, suggesting their small charge transfer resistances. The largest tilt of RuCoN$_x$/C in the mid-frequency region implies the smallest Warburg impedance, which arises from the limited ion transport, indicating the highest diffusion rate among all samples. The low-frequency region of the Bode plot reveals the features related to oxygen diffusion limitation. All catalysts display similar large phase angles, indicative of high accessibility for solvated reactants thanks to their hierarchical pores. Double-layer capacitance (C_{dl}) is a useful index to describe the electrochemical surface area and mass diffusion property of catalysts. RuMN$_x$/C catalysts share similar C_{dl} values (*ca*. 19.4 ± 1.7 mF cm^{-2}) owing to the same synthetic approach (**Figure S25**), which is consistent

with the electron microscopic characterizations of structure and morphology. These similarities in structure and mass transport properties of $RuMN_x/C$ catalysts signify that their different ORR behaviors originate from their intrinsic activity of atomic sites.

To better distinguish the intrinsic kinetic properties of Ru–M sites, a gas diffusion flow cell was utilized to circumvent the mass transfer-limited ORR caused by the low concentration of dissolved oxygen in the electrolyte. By conducting the ORR at the triple-phase in a gas diffusion flow cell, the conditions in practical applications such as fuel cell and metal–air battery can be simulated (**Figure S26** and **Note S5**).[33] **Figure 4d** shows the polarization curves recorded using the flow cell from 1.0 to 0.6 V *vs*. RHE where the difference of $RuMN_x/C$ catalysts in their catalytic activities at lower potentials are clearly revealed. In particular, the introduction of dual atomic Ru–Co sites apparently improves the ORR activity of the single atomic one (RuN_x/C) as manifested by a 90-mV shift in onset potential and a 16-fold current increment at 0.75 V. Other dual atomic catalysts also exhibit enhanced catalytic ORR performances, confirming the positive impact of atomic site engineering on the ORR activity.

Turnover frequency (TOF) is one of the key criteria for intrinsic activity evaluation and can be calculated from the catalytic current normalized by the total number of active sites. However, the quantification of active sites in various electrocatalysts poses an experimental challenge, a problem that is also complicated by the spectator metal sites in high-loading SACs.[34, 35] In our case, a similar metal loading of *ca*. 0.5 wt.% was determined for all samples by ICP-OES and used for the calculation of TOF assuming 100 % participation in ORR (**Note S6**). The current densities at 0.8 and 0.7 V *vs*. RHE were selected for a quantitative investigation on how the di-atomic coupling in Ru–M pairs impacts the ORR activity. **Figure 4e** compares the TOF values obtained from RuN_x/C and $RuMN_x/C$ catalysts. It is clear that the TOF value is largely affected by the type of second 3*d*

metal, showing a trend of $RuCoN_x/C > RuFeN_x/C > RuNiN_x/C > RuN_x/C$. The result indicates the "pulling effect" of $3d$ metals on Ru site owing to their different electron-withdrawing abilities. Notably, the $RuCoN_x/C$ records the TOFs of 2.424 and 0.313 s^{-1} at 0.8 and 0.7 V, showing 704 and 680 % enhancements from RuN_x/C, respectively. The durability of $RuCoN_x/C$ was assessed by a long-term chronoamperometric test as shown in **Figure S27a**, which displays a good current retainment of 89.4 % for 20 h, which is better than Pt/C (86.1 %). After 500 cycling of ORR, $RuCoN_x/C$ shows a negligible decline in the halfwave potential, and it also demonstrates excellent methanol tolerance exceeding that of Pt/C. The Raman and TEM characterizations after ORR (**Figures S27b** – **S27d**) indicate the structural durability of $RuCoN_x/C$ under ORR conditions.

The reversibility of ORR electrodes, *i.e.*, their capability of catalyzing oxygen evolution reaction (OER), is of crucial importance for the advancement of rechargeable metal−air batteries and fuel cells that involve these two reversible reactions.[36] We tested the electrochemical OER property of $RuCoN_x/C$ using a two-electrode cell in O_2-saturated 1 M KOH. Notably, $RuCoN_x/C$ also serves as a superb catalyst toward the OER with a small overpotential of 0.268 V at 10 mA cm^{-2} (without *i*R compensation) and surpasses the performance of most reported SACs.[6, 22] The high operational potential of OER may cause the activity degradation of atomic catalysts. The OER stability of $RuCoN_x/C$ was investigated by a combination of Raman spectroscopy, *operando* ICP-OES, and aberration-corrected HAADF-STEM (**Figure S28**). $RuCoN_x/C$ maintains a stable current response at 1.5 V without any serious carbon corrosion, demetallation, and agglomeration. The polarization curve of $RuCoN_x/C$ in the full cell demonstrates its excellent bifunctional activity towards overall OER/ORR among all catalysts. The difference between its $E_{1/2}$ for ORR and OER potential at 10 mA cm^{-2} is merely 0.603 V, which is much smaller than those of $Pt/C|RuO_2$ (0.675 V) and other analogues (**Figure S29a**).

With excellent reversibility as the oxygen electrode, RuCoN$_x$/C was utilized as the working electrode in a rechargeable Zn–air battery. The discharge/charge behavior of the RuCoN$_x$/C electrode was evaluated as shown in **Figure 4f**. The RuCoN$_x$/C electrode delivers a higher discharging voltage (*e.g.*, 0.96 V at 100 mA cm^{-2}) and a lower charging voltage (*e.g.*, 2.14 V at 100 mA cm^{-2}) than the Pt/C|RuO$_2$ commercial catalyst system (0.83 and 2.32 V, respectively), demonstrating a good performance as the air electrode in Zn–air battery. Moreover, the RuCoN$_x$/C electrode achieves a larger peak power density of 130 mW cm^{-2} compared with Pt/C|RuO$_2$ (90 mW cm^{-2}). To evaluate the cycling rechargeability, the battery assembled with the RuCoN$_x$/C electrode was cycled at a discharge/charge current density of 2 mA cm^{-2} (**Figure S29b**). The RuCoN$_x$/C electrode shows great durability and outperforms the Pt/C|RuO$_2$ electrode (0.656 V) with a small voltage gap of 0.603 V and negligible voltage fading after continuous operation of 140 cycles (70 h). The Radar chart in **Figure S29c** summarizes their ORR and Zn–air battery performances, which suggests the superior behaviors of RuCoN$_x$/C in half-cell reaction and the practical application.

Density functional theory (DFT) calculations were performed to further understand the activity of dimeric metal sites toward ORR electrocatalysis. A series of models of Ru–M (M = Fe, Co, and Ni) sites and single atoms (Fe, Co, Ni, and Ru) located in the graphene substrate were established (**Figure S30**). The adsorption energies of oxygenated intermediates for all systems were subsequently calculated. As mentioned before, Ru-based SACs generally have too strong binding strength towards the intermediates, and thus a strategy to lower the binding strength should be applied.[24] Considering the interatomic distance (2.09 ± 0.25 Å) and coordination number (Ru–N and Co–N are 2.35 and 2.63, respectively) of our dual-metal catalysts, RuMN$_6$ models were adopted as model systems. Accordingly, another possible model (RuMN$_6$-2) was excluded because

of the adsorption energy (ΔE_{ads}) of OH ranging from -0.21 to 0.32 eV, which is too low for OH to be desorbed for both two- and four-electron pathways (**Table S5**).
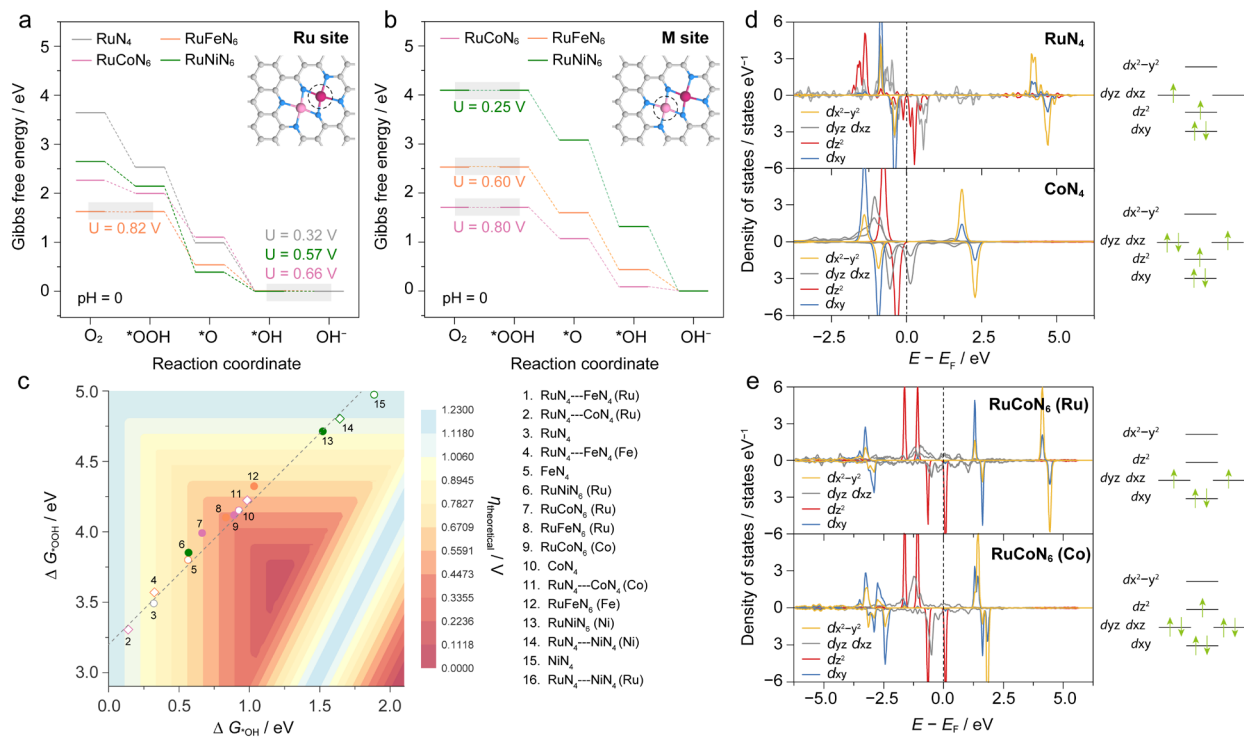
Figure 5. Reaction free energy diagrams of RuMN$_6$ (M = Co, Fe, Ni) for ORR at respective onset potential (*U*). Intermediates are adsorbed on (a) Ru site or (b) M site. (c) 2D activity map (U = 0 V *vs.* RHE) with the Gibbs free energies of *OH (ΔG_{*OH}) and *OOH (ΔG_{*OOH}) as the first and second descriptors, respectively. The dotted line indicates the linear scaling relationship between ΔG_{*OOH} and ΔG_{*OH}. Projected density of states of *d* orbitals for modeling structures. (d), RuN$_4$, CoN$_4$, and (e), RuCoN$_6$. The diagrams on the right represent their electron configurations.

First, we evaluated the catalytic performance of single metal sites (**Figure S31a**). FeN$_4$ and RuN$_4$ have over-binding of intermediates, while NiN$_4$ shows a weak adsorption strength. Among the single metal sites investigated, CoN$_4$ is expected to show the best ORR performance with a theoretical overpotential (η) of 0.45 V in accordance with the previous report.[37] Dimeric interactions of center metals are weak for RuN$_4$---MN$_4$ systems such that the change in adsorption affinity towards the intermediates for the respective metal sites is insignificant (**Figures S31b** and

17

S31c). The free energy diagrams of ORR for the Ru−M dual metal sites of RuMN$_6$ were further compared on Ru and M sites. For Ru sites (**Figures 5a** and **S32a**), RuFeN$_6$ shows the best ORR performance and the rate-determining step (RDS) of O$_2$ → *OOH (1st step). However, the weak adsorption energy of O$_2$ (4.86 eV) on the Ru site can be kinetically detrimental (**Table S6**).[38] The Ru sites on other dimers have inferior performance with the RDS of *OH → 4OH$^-$ (4th step). The decrease in η of RuCoN$_6$ and RuNiN$_6$ compared with that of RuN$_4$ indicates that the binding strength of the intermediates on Ru site is weakened by the introduction of the second metal species. The free energy diagram of ORR at M site (**Figures 5b** and **S32b**) shows that RuCoN$_6$ exhibits the best performance with the η of 0.43 V among all systems investigated. The 3D activity map obtained by plotting the calculated η against the first and second descriptors ΔG_{*OH} and ΔG_{*OOH} (**Figure 5c**) clearly reveals the optimum binding strength of intermediates for the Co site of RuCoN$_6$.

In order to reveal the underlying reason for the modulation of catalytic activity, the electronic structure of RuCoN$_6$ was first investigated and compared with its single atomic counterparts. For square planar coordination of D_{4h} symmetry, the d_{xz}, d_{yz}, and d_{z^2} states of transition metal center are more stabilized due to the absence of z-direction ligands. The order of energy levels can be changed with the type of ligand and the bond length between the metal center and ligand. For example, σ-donor ligands and shortened metal−ligand bond length lead to the participation of the torus-shaped a_{1g} orbital, resulting in the unstable d_{z^2}.[39] **Figure 5d** shows the projected density of states (DOS) of d-orbitals of single atomic Ru and Co sites. For both Ru and Co, high asymmetric unfilled d-orbital energy levels of d_{xz} and d_{yz} are observed. For the dual metal sites (**Figure 5e**), d_{xz} and d_{yz} orbital peaks are reduced for Ru and Co. It is interesting to note that unfilled d_{z^2} orbital peaks appear near the Fermi level, which indicates the rearrangement of the d-orbital energy levels.

Such a decrease in asymmetric peaks signifies the decrease in the magnetic moment in the projector-augmented-wave (PAW) sphere (**Figures 5d** and **5e**), which may regulate the catalytic performance.[35, 38] The crystal orbital Hamilton populations (COHP) analysis was also carried out to understand the binding strengths of key intermediates (OH), and the results are summarized in **Figure S34**. All systems show the filling of antibonding states in d orbital energy states. The absolute values of integrated COHP (ICOHP) are 3.53, 2.42, 3.11, and 3.54 for RuN_4, CoN_4, $RuCoN_6$ (Ru), and $RuCoN_6$ (Co), respectively. The different extents of the antibonding state-filling also validate the binding strengths change of OH* (**Table S6**). The Ru site in $RuCoN_6$ has a weaker affinity toward the OH compared with that in RuN_4, while the Co in $RuCoN_6$ has a stronger affinity than that in CoN_4. Moreover, the charge state of the metal components by Bader analysis indicates that Ru loses the charge (Ru in RuN_4 is 1.30 and Ru in $RuCoN_6$ is 0.99).[40] To conclude, the reduction of magnetic moment and charge state of $RuCoN_6$ induce the decrease in d-band center energy, which leads to the weaker adsorption energy towards the intermediates and further improvement in ORR performance. Such analyses on the optimization of electronic structure and its correlation with catalytic performance are also applicable to Ru–Fe(Ni) di-atomic sites and their single-atomic counterparts (see the d-band center, DOS, and Bader charge analysis in **Note S7**, **Figures S35 – 38**, and **Table S7**).

Conclusions

In summary, ORR performance and mechanism of Ru–M di-atomic structures including controllable synthesis, microscopic, spectroscopic, electrochemical techniques, and computational simulations were studied by an integrated investigation. We described a delicate "encapsulation-substitution" strategy to form binuclear sites in the ordered macroporous N-doped carbon. The

results revealed how the ORR activity of Ru atom was modulated by changes in electronic structures with the introduction of the secondary $3d$ metal atom. This work provides a clear understanding of how dimer moiety affects the oxygen-involved reaction processes with an emphasis on the importance of site-to-site interaction and thus provides insightful guidance on the design and application of dual atomic catalysts.

METHODS

Chemicals. Potassium hydroxide (99.99 %), potassium persulfate (99.0 %), polyvinyl pyrrolidone (average MW = 10,000 g mol^{-1}), sodium hydroxide (90 %), 2-methylimidazole (99 %), zinc nitrate hexahydrate ($Zn(NO_3)_2 \cdot 6H_2O$, 98 %), ruthenium acetylacetonate ($Ru(acac)_3$, 97 %), cobalt nitrate hexahydrate ($Co(NO_3)_2 \cdot 6H_2O$, 98 %), nickel nitrate hexahydrate ($Ni(NO_3)_2 \cdot 6H_2O$, 98 %), iron nitrate nonahydrate ($Fe(NO_3)_2 \cdot 9H_2O$, 98 %), dimethylformamide (DMF, >99.8 %), Pt/C (20 wt.%), and RuO_2 were purchased from Sigma−Aldrich. Methanol, ammonia aqueous solution ($NH_3 \cdot H_2O$), and styrene were purchased from Tokyo Chemical Industry (TCI).

Preparation of Ordered Porous Ru@ZnCo-ZIF. Ru@ZnCo-ZIF microcrystals were fabricated through an impregnation process in the presence of ordered polystyrene (PS) monoliths that was synthesized according to a reported procedure.[9] To a methanolic solution (50 mL) containing 2-methylimidazole (80 mmol), $Zn(NO_3)_2$ (20 mmol), $Ru(acac)_3$ (0.1 mmol), and $Co(NO_3)_2$ (0.1 mmol), the ordered PS template (5 g) was immersed under vacuum degassing for 10 min. After 1 h of immersion, the precursor-adsorbed PS was taken out, dried at 50 °C, and then soaked in a mixed solution of CH_3OH and $NH_3 \cdot H_2O$ (1:1 v/v) under vacuum degassing for 5 min before sitting at atmospheric pressure overnight. The PS template was removed by washing with DMF several times to afford the Ru@ZnCo-ZIF microcrystals. For Ru@ZnCo-ZIFs with higher Ru and Co contents, the same procedure was taken except that higher $Ru(acac)_3$ and $Co(NO_3)_2$ concentrations

of 0.2 and 0.3 mmol were used, and the products were denoted as Ru@ZnCo-ZIF-2 and Ru@ZnCo-ZIF-3, respectively. The other two bimetallic ZIFs, Ru@ZnFe-ZIF and Ru@ZnNi-ZIF, were synthesized in the same way by replacing $Co(NO_3)_2$ with $Fe(NO_3)_3$ and $Ni(NO_3)_2$, respectively, and Ru@Zn-ZIF was prepared without $Co(NO_3)_2$.

Preparation of Ordered Porous $RuCoN_x/C$. $RuCoN_x/C$ was prepared by pyrolysis of Ru@ZnCo-ZIF at 950 °C under argon flow (100 sccm, 5 oC min^{-1}) for 2 h. Other single/dual atomic samples were prepared by the same calcination treatment of Ru@ZnFe-ZIF, Ru@ZnNi-ZIF, and Ru@Zn-ZIF, which are denoted as $RuFeN_x/C$, $RuNiN_x/C$, and RuN_x/C, respectively. RuCo cluster and particle samples were prepared by pyrolyzing Ru@ZnCo-ZIF-2 and Ru@ZnCo-ZIF-3, respectively.

ASSOCIATED CONTENT

Supporting Information Available

Optical and SEM images of PS template; XRD patterns and SEM images of Ru@ZnM-ZIF; XRD patterns, SEM, TEM, HAADF-STEM image, XAFS and XPS analysis of $RuMN_X/C$; electrochemical ORR measurements including CV, LSV, Tafel plot, Arrhenius plot, K–L plot, rate constant, Nyquist plot, Bode plot, flow cell kinetic study, amperometry and Zn–Air battery test; theoretical model for DFT calculation, reaction free energy diagram, volcano plot, COHP analysis, d-band center energy, PDOS and Bader charge.

AUTHOR INFORMATION

Corresponding Authors

Chia-Min Yang (cmyang@mx.nthu.edu.tw): Department of Chemistry, National Tsing Hua University, Hsinchu 300034, Taiwan; Frontier Research Center on Fundamental and Applied

Sciences of Matters, National Tsing Hua University, Hsinchu 300034, Taiwan. ORCID: 0000-0001-9990-4779.

Byungchan Han (bchan@yonsei.ac.kr): Department of Chemical and Biomolecular Engineering, Yonsei University, Seoul 03722, Republic of Korea. ORCID: 0000-0002-2325-6733.

Lawrence Yoon Suk Lee (lawrence.ys.lee@polyu.edu.hk): Department of Applied Biology and Chemical Technology and the State Key Laboratory of Chemical Biology and Drug Discovery, The Hong Kong Polytechnic University, Hung Hom, Kowloon, Hong Kong SAR, China; Research Institute for Smart Energy, The Hong Kong Polytechnic University, Hung Hom, Kowloon, Hong Kong SAR, China. ORCID: 0000-0002-6119-4780.

Authors

Mengjie Liu: Department of Applied Biology and Chemical Technology and the State Key Laboratory of Chemical Biology and Drug Discovery, The Hong Kong Polytechnic University, Hung Hom, Kowloon, Hong Kong SAR, China. ORCID: 0000-0002-7855-8763.

Hoje Chun: Department of Chemical and Biomolecular Engineering, Yonsei University, Seoul 03722, Republic of Korea.

Tsung-Cheng Yang: Department of Chemistry, National Tsing Hua University, Hsinchu 300034, Taiwan.

Sung Jun Hong: Department of Chemical and Biomolecular Engineering, Yonsei University, Seoul 03722, Republic of Korea.

Author Contributions

M.J. Liu and L.Y.S. Lee conceived and designed the project. M.J. Liu synthesized, measured, and analyzed the samples. T.C. Yang measured and analyzed the X-ray absorption spectroscopic data. H. Chun and S.J. Hong performed the theoretical calculations. M.J. Liu and L.Y.S. Lee performed

data visualization and wrote the manuscript. C.M. Yang, B. Han, and L.Y.S. Lee supervised the project. All authors discussed the results and provided comments and advices on the manuscript.

Notes

The authors declare no competing financial interest.

REFERENCES

1. Wang, A.; Li, J.; Zhang, T., Heterogeneous Single-Atom Catalysis. *Nat. Rev. Chem.* **2018**, *2*, 65-81.

2. Li, Z.; Chen, Y.; Ji, S.; Tang, Y.; Chen, W.; Li, A.; Zhao, J.; Xiong, Y.; Wu, Y.; Gong, Y.; Yao, T.; Liu, W.; Zheng, L.; Dong, J.; Wang, Y.; Zhuang, Z.; Xing, W.; He, C.-T.; Peng, C.; Cheong, W.-C.; Li, Q.; Zhang, M.; Chen, Z.; Fu, N.; Gao, X.; Zhu, W.; Wan, J.; Zhang, J.; Gu, L.; Wei, S.; Hu, P.; Luo, J.; Li, J.; Chen, C.; Peng, Q.; Duan, X.; Huang, Y.; Chen, X.-M.; Wang, D.; Li, Y., Iridium Single-Atom Catalyst on Nitrogen-Doped Carbon for Formic Acid Oxidation Synthesized Using A General Host–Guest Strategy. *Nat. Chem.* **2020**, *12*, 764-772.

3. Chu, C.; Huang, D.; Gupta, S.; Weon, S.; Niu, J.; Stavitski, E.; Muhich, C.; Kim, J.-H., Neighboring Pd Single Atoms Surpass Isolated Single Atoms for Selective Hydrodehalogenation Catalysis. *Nat. Commun.* **2021**, *12*, 5179.

4. Gu, J.; Hsu, C.-S.; Bai, L.; Chen Hao, M.; Hu, X., Atomically Dispersed Fe^{3+} Sites Catalyze Efficient CO_2 Electroreduction to CO. *Science* **2019**, *364*, 1091-1094.

5. Xiao, M.; Xing, Z.; Jin, Z.; Liu, C.; Ge, J.; Zhu, J.; Wang, Y.; Zhao, X.; Chen, Z., Preferentially Engineering FeN_4 Edge Sites onto Graphitic Nanosheets for Highly Active and Durable Oxygen Electrocatalysis in Rechargeable Zn–Air Batteries. *Adv. Mater.* **2020**, *32*, 2004900.

6. Fei, H.; Dong, J.; Feng, Y.; Allen, C. S.; Wan, C.; Volosskiy, B.; Li, M.; Zhao, Z.; Wang, Y.; Sun, H.; An, P.; Chen, W.; Guo, Z.; Lee, C.; Chen, D.; Shakir, I.; Liu, M.; Hu, T.; Li, Y.; Kirkland, A. I.; Duan, X.; Huang, Y., General Synthesis and Definitive Structural

Identification of MN_4C_4 Single-Atom Catalysts with Tunable Electrocatalytic Activities. *Nat. Catal.* **2018**, *1*, 63-72.

7. Meng, F.-L.; Liu, K.-H.; Zhang, Y.; Shi, M.-M.; Zhang, X.-B.; Yan, J.-M.; Jiang, Q., Recent Advances toward the Rational Design of Efficient Bifunctional Air Electrodes for Rechargeable Zn–Air Batteries. *Small* **2018**, *14*, 1703843.

8. Meng, F.; Zhong, H.; Bao, D.; Yan, J.; Zhang, X., In Situ Coupling of Strung Co_4N and Intertwined N–C Fibers toward Free-Standing Bifunctional Cathode for Robust, Efficient, and Flexible Zn–Air Batteries. *J. Am. Chem. Soc.* **2016**, *138*, 10226-10231.

9. Jiang, R.; Li, L.; Sheng, T.; Hu, G.; Chen, Y.; Wang, L., Edge-Site Engineering of Atomically Dispersed Fe–N_4 by Selective C–N Bond Cleavage for Enhanced Oxygen Reduction Reaction Activities. *J. Am. Chem. Soc.* **2018**, *140*, 11594-11598.

10. Wang, X.; Chen, Z.; Zhao, X.; Yao, T.; Chen, W.; You, R.; Zhao, C.; Wu, G.; Wang, J.; Huang, W.; Yang, J.; Hong, X.; Wei, S.; Wu, Y.; Li, Y., Regulation of Coordination Number over Single Co Sites: Triggering the Efficient Electroreduction of CO_2. *Angew. Chem. Int. Ed.* **2018**, *57*, 1944-1948.

11. Choi, C. H.; Kim, M.; Kwon, H. C.; Cho, S. J.; Yun, S.; Kim, H.-T.; Mayrhofer, K. J. J.; Kim, H.; Choi, M., Tuning Selectivity of Electrochemical Reactions by Atomically Dispersed Platinum Catalyst. *Nat. Commun.* **2016**, *7*, 10922.

12. Li, W.; Zhao, Y.; Liu, Y.; Sun, M.; Waterhouse, G. I. N.; Huang, B.; Zhang, K.; Zhang, T.; Lu, S., Exploiting Ru-Induced Lattice Strain in CoRu Nanoalloys for Robust Bifunctional Hydrogen Production. *Angew. Chem. Int. Ed.* **2021**, *60*, 3290-3298.

13. Zhao, L.; Zhang, Y.; Huang, L.-B.; Liu, X.-Z.; Zhang, Q.-H.; He, C.; Wu, Z.-Y.; Zhang, L.-J.; Wu, J.; Yang, W.; Gu, L.; Hu, J.-S.; Wan, L.-J., Cascade Anchoring Strategy for General

Mass Production of High-Loading Single-Atomic Metal-Nitrogen Catalysts. *Nat. Commun.* **2019**, *10*, 1278.

14. Xia, C.; Qiu, Y.; Xia, Y.; Zhu, P.; King, G.; Zhang, X.; Wu, Z.; Kim, J. Y.; Cullen, D. A.; Zheng, D.; Li, P.; Shakouri, M.; Heredia, E.; Cui, P.; Alshareef, H. N.; Hu, Y.; Wang, H., General Synthesis of Single-atom Catalysts with High Metal Loading Using Graphene Quantum Dots. *Nat. Chem.* **2021**, *13*, 887-894.

15. Pan, Y.; Zhang, C.; Liu, Z.; Chen, C.; Li, Y., Structural Regulation with Atomic-Level Precision: From Single-Atomic Site to Diatomic and Atomic Interface Catalysis. *Matter* **2020**, *2*, 78-110.

16. Lu, Z.; Wang, B.; Hu, Y.; Liu, W.; Zhao, Y.; Yang, R.; Li, Z.; Luo, J.; Chi, B.; Jiang, Z.; Li, M.; Mu, S.; Liao, S.; Zhang, J.; Sun, X., An Isolated Zinc–Cobalt Atomic Pair for Highly Active and Durable Oxygen Reduction. *Angew. Chem. Int. Ed.* **2019**, *58*, 2622-2626.

17. Zhang, N.; Zhou, T.; Ge, J.; Lin, Y.; Du, Z.; Zhong, C. a.; Wang, W.; Jiao, Q.; Yuan, R.; Tian, Y.; Chu, W.; Wu, C.; Xie, Y., High-Density Planar-like Fe_2N_6 Structure Catalyzes Efficient Oxygen Reduction. *Matter* **2020**, *3*, 509-521.

18. Xiao, M.; Chen, Y.; Zhu, J.; Zhang, H.; Zhao, X.; Gao, L.; Wang, X.; Zhao, J.; Ge, J.; Jiang, Z.; Chen, S.; Liu, C.; Xing, W., Climbing the Apex of the ORR Volcano Plot via Binuclear Site Construction: Electronic and Geometric Engineering. *J. Am. Chem. Soc.* **2019**, *141*, 17763-17770.

19. Miao, Q.; Yang, S.; Xu, Q.; Liu, M.; Wu, P.; Liu, G.; Yu, C.; Jiang, Z.; Sun, Y.; Zeng, G., Constructing Synergistic $Zn-N_4$ and $Fe-N_4O$ Dual-Sites from the COF@MOF Derived Hollow Carbon for Oxygen Reduction Reaction. *Small Structures* **2022**, *3*, 2100225.

20. Ji, S.; Chen, Y.; Fu, Q.; Chen, Y.; Dong, J.; Chen, W.; Li, Z.; Wang, Y.; Gu, L.; He, W.; Chen, C.; Peng, Q.; Huang, Y.; Duan, X.; Wang, D.; Draxl, C.; Li, Y., Confined Pyrolysis within Metal–Organic Frameworks To Form Uniform Ru_3 Clusters for Efficient Oxidation of Alcohols. *J. Am. Chem. Soc.* **2017**, *139*, 9795-9798.

21. Escudero-Escribano, M.; Malacrida, P.; Hansen Martin, H.; Vej-Hansen Ulrik, G.; Velázquez-Palenzuela, A.; Tripkovic, V.; Schiøtz, J.; Rossmeisl, J.; Stephens Ifan, E. L.; Chorkendorff, I., Tuning the Activity of Pt Alloy Electrocatalysts by Means of the Lanthanide Contraction. *Science* **2016**, *352*, 73-76.

22. Cao, L.; Luo, Q.; Chen, J.; Wang, L.; Lin, Y.; Wang, H.; Liu, X.; Shen, X.; Zhang, W.; Liu, W.; Qi, Z.; Jiang, Z.; Yang, J.; Yao, T., Dynamic Oxygen Adsorption on Single-Atomic Ruthenium Catalyst with High Performance for Acidic Oxygen Evolution Reaction. *Nat. Commun.* **2019**, *10*, 4849.

23. Precious Metal Price Charts. http://www.platinum.matthey.com/prices (accessed on 26 December 2021).

24. Xiao, M.; Gao, L.; Wang, Y.; Wang, X.; Zhu, J.; Jin, Z.; Liu, C.; Chen, H.; Li, G.; Ge, J.; He, Q.; Wu, Z.; Chen, Z.; Xing, W., Engineering Energy Level of Metal Center: Ru Single-Atom Site for Efficient and Durable Oxygen Reduction Catalysis. *J. Am. Chem. Soc.* **2019**, *141*, 19800-19806.

25. Gao, G.; Waclawik, E. R.; Du, A., Computational Screening of Two-Dimensional Coordination Polymers as Efficient Catalysts for Oxygen Evolution and Reduction Reaction. *J. Catal.* **2017**, *352*, 579-585.

26. Wang, X.; Zhang, H.; Lin, H.; Gupta, S.; Wang, C.; Tao, Z.; Fu, H.; Wang, T.; Zheng, J.; Wu, G.; Li, X., Directly Converting Fe-Doped Metal–Organic Frameworks into Highly Active and Stable Fe-N-C Catalysts for Oxygen Reduction in Acid. *Nano Energy* **2016**, *25*, 110-119.

27. Yin, P.; Yao, T.; Wu, Y.; Zheng, L.; Lin, Y.; Liu, W.; Ju, H.; Zhu, J.; Hong, X.; Deng, Z.; Zhou, G.; Wei, S.; Li, Y., Single Cobalt Atoms with Precise N-Coordination as Superior Oxygen Reduction Reaction Catalysts. *Angew. Chem. Int. Ed.* **2016**, *55*, 10800-10805.

28. Highfield, J.; Liu, T.; Loo, Y. S.; Grushko, B.; Borgna, A., Skeletal Ru/Cu catalysts prepared from crystalline and quasicrystalline ternary alloy precursors: characterization by X-ray absorption spectroscopy and CO oxidation. *Phys. Chem. Chem. Phys.* **2009**, *11*, 1196-1208.

29. Yao, Y.; Hu, S.; Chen, W.; Huang, Z.-Q.; Wei, W.; Yao, T.; Liu, R.; Zang, K.; Wang, X.; Wu, G.; Yuan, W.; Yuan, T.; Zhu, B.; Liu, W.; Li, Z.; He, D.; Xue, Z.; Wang, Y.; Zheng, X.; Dong, J.; Chang, C.-R.; Chen, Y.; Hong, X.; Luo, J.; Wei, S.; Li, W.-X.; Strasser, P.; Wu, Y.; Li, Y., Engineering the Electronic Structure of Single Atom Ru Sites *via* Compressive Strain Boosts Acidic Water Oxidation Electrocatalysis. *Nat. Catal.* **2019**, *2*, 304-313.

30. Osmieri, L.; Monteverde Videla, A. H. A.; Ocón, P.; Specchia, S., Kinetics of Oxygen Electroreduction on Me–N‑C (Me = Fe, Co, Cu) Catalysts in Acidic Medium: Insights on the Effect of the Transition Metal. *J. Phys. Chem. C* **2017**, *121*, 17796-17817.

31. Damjanovic, A.; Genshaw, M. A.; Bockris, J. O. M., Distinction between Intermediates Produced in Main and Side Electrodic Reactions. *J. Chem. Phys.* **1966**, *45*, 4057-4059.

32. Wu, F.; Pan, C.; He, C.-T.; Han, Y.; Ma, W.; Wei, H.; Ji, W.; Chen, W.; Mao, J.; Yu, P.; Wang, D.; Mao, L.; Li, Y., Single-Atom Co–N_4 Electrocatalyst Enabling Four-Electron Oxygen Reduction with Enhanced Hydrogen Peroxide Tolerance for Selective Sensing. *J. Am. Chem. Soc.* **2020**, *142*, 16861-16867.

33. Inaba, M.; Jensen, A. W.; Sievers, G. W.; Escudero-Escribano, M.; Zana, A.; Arenz, M., Benchmarking High Surface Area Electrocatalysts in A Gas Diffusion Electrode: Measurement of Oxygen Reduction Activities under Realistic Conditions. *Energy Environ. Sci.* **2018**, *11*, 988-994.

34. Anantharaj, S.; Karthik, P. E.; Noda, S., The Significance of Properly Reporting Turnover Frequency in Electrocatalysis Research. *Angew. Chem. Int. Ed.* **2021**, *60*, 23051-23067.

35. Jin, Z.; Li, P.; Meng, Y.; Fang, Z.; Xiao, D.; Yu, G., Understanding the Inter-Site Distance Effect in Single-Atom Catalysts for Oxygen Electroreduction. *Nat. Catal.* **2021**, *4*, 615-622.

36. Ma, T. Y.; Dai, S.; Jaroniec, M.; Qiao, S. Z., Metal–Organic Framework Derived Hybrid Co_3O_4-Carbon Porous Nanowire Arrays as Reversible Oxygen Evolution Electrodes. *J. Am. Chem. Soc.* **2014**, *136*, 13925-13931.

37. Jung, E.; Shin, H.; Lee, B.-H.; Efremov, V.; Lee, S.; Lee, H. S.; Kim, J.; Hooch Antink, W.; Park, S.; Lee, K.-S.; Cho, S.-P.; Yoo, J. S.; Sung, Y.-E.; Hyeon, T., Atomic-Level Tuning of Co–N–C Catalyst for High-Performance Electrochemical H_2O_2 Production. *Nat. Mater.* **2020**, *19*, 436-442.

38. Yang, G.; Zhu, J.; Yuan, P.; Hu, Y.; Qu, G.; Lu, B.-A.; Xue, X.; Yin, H.; Cheng, W.; Cheng, J.; Xu, W.; Li, J.; Hu, J.; Mu, S.; Zhang, J.-N., Regulating Fe-Spin State by Atomically Dispersed Mn-N in Fe-N-C Catalysts with High Oxygen Reduction Activity. *Nat. Commun.* **2021**, *12*, 1734.

39. Börgel, J.; Campbell, M. G.; Ritter, T., Transition Metal *d*-Orbital Splitting Diagrams: An Updated Educational Resource for Square Planar Transition Metal Complexes. *J. Chem. Educ.* **2016**, *93*, 118-121.

40. Henkelman, G.; Arnaldsson, A.; Jónsson, H., A Fast and Robust Algorithm for Bader Decomposition of Charge Density. *Comput. Mater. Sci.* **2006**, *36*, 354-360.

TABLE OF CONTENTS
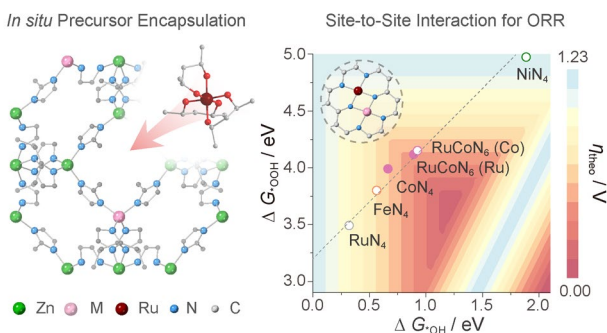
A delicate "precursor encapsulation–ZIF metal node substitution" strategy was proposed for the synthesis of paired metal sites in N-doped carbon. With the regulation of *d*-orbital energy level, a significant increment in oxygen electroreduction activity was demonstrated in Ru–Co di-atomic catalyst (DAC) than its single atomic counterparts. The Ru–Co DAC efficiently reduces oxygen with a high turnover frequency of 2.424 s^{-1} at 0.7 V, establishing optimal thermodynamic and kinetic behaviors in the triple-phase reaction in a flow cell. Our findings provide a clear understanding of site-to-site interaction on ORR and a benchmark evaluation of atomic catalysts with correlations of di-atomic structure, energy level, and whole catalytic performance at the sub-nanometer level.